



Experimental Investigation of Single Bubble Nucleate Boiling in Microgravity

Iman Nejati¹ · Axel Sielaff¹ · Benjamin Franz¹ · Matthias Zimmermann¹ · Philipp Hänichen¹ · Kai Schweikert¹ · Julian Krempel¹ · Peter Stephan¹ · Anne Martin² · Herbert Scheerer² · Tom Engler² · Matthias Oechsner²

Received: 16 December 2019 / Accepted: 18 June 2020 / Published online: 4 July 2020
© Springer Nature B.V. 2020

Abstract

The *multiscale boiling* project, also known as RUBI, is an experimental project supported by the European Space Agency (ESA) focusing on the nucleate boiling within the framework of the utilization of the International Space Station (ISS). In order to investigate the operational behavior of the experimental components and determine a promising parameter range, an experimental setup with the same heater design is constructed and tested within the similar parameter range in the framework of the ESA 70th parabolic flight campaign. The present work introduces the experimental setup as well as the measurement methodologies. It concentrates on the results obtained for the nucleate boiling in the absence of external forces such as electric field or shear flow, which are also part of the *multiscale boiling* project. A barium fluoride glass sputtered with chromium on the top of a chromium nitride layer served as the heater. The manufacturing process of the heater substrate is presented in detail. In order to generate a vapor bubble in the subcooled liquid pool, a laser beam is used to provide the necessary heat at an artificial nucleation site situated at the center of the glass. The experimental setup allows for time adjustment between switch-on of the heater and shooting the laser which is defined as preheating time. The effect of the preheating time on the nucleation and behavior of the bubbles is investigated. Furthermore, by selecting a long laser pulse duration the influence of the laser thermal energy on the growth of the bubbles is studied. It is observed that the preheating time has a significant effect on the bubble growth. However, no influence of the laser shot is detected on the bubble growth, even for a long pulse duration.

Keywords Nucleate boiling · Microgravity · Multiscale boiling · RUBI

Introduction

Boiling is a promising heat transfer mechanism, which is omnipresent in a variety of engineering fields such as food

and chemical process industries as well as air conditioning systems and cooling units. These systems take advantage of latent heat transportation, which generally enables a good efficiency for heat exchangers. Boiling heat transfer systems are not only used widely in terrestrial environments, but also are considered as extremely beneficial for space applications. Based on rapidly growing power requirements of on-board electronic devices for space missions, there is a high demand for an efficient heat removal system in the lack of natural convection in the zero gravity environment. Since boiling is a highly efficient heat transfer mechanism occurring at relatively small temperature differences, it becomes of great importance for the design of heat exchangers for future planetary missions.

Despite of the wide range of applications, boiling has not been sufficiently understood yet. The main reason is the complex physical phenomena governing the heat and mass transport combined with hydrodynamics and interfacial processes. Numerous scientific studies have been

This article belongs to the Topical Collection: Multiphase Fluid Dynamics in Microgravity
Guest Editors: Tatyana P. Lyubimova, Jian-Fu Zhao

✉ Iman Nejati
iman.nejati@gmail.com

Matthias Oechsner
oechsner@mpa-ifw.tu-darmstadt.de

- ¹ Institute for Technical Thermodynamics, Technische Universität Darmstadt, Alarich-Weiss-Strasse 10, 64287 Darmstadt, Germany
- ² State Material Testing Institute Darmstadt, Institute for Material Technology, surface Technology and Corrosion, Technische Universität Darmstadt, Grafenstr. 2, 64283 Darmstadt, Germany

devoted e.g. to determine the departure diameter of a vapor bubble under terrestrial conditions (Fritz 1935; Cole 1967; Cole and Rohsenow 1969; Schweizer 2010). On ground, however, buoyancy often superimposes or even totally masks other transport phenomena. Thus, it is hard or even impossible to observe them. By contrary, under reduced gravitational conditions experiments allow such observations. In this case, the effects like inertia forces or bubble coalescence become dominant for the bubble departure process (Straub et al. 1992). Moreover, the boiling process is decelerated under reduced gravitational conditions. Thereby the observation using the available measurement technologies leads to a higher spatial and temporal resolution related to the characteristic length and time scales of the transport phenomena.

A significant amount of heat provided to a growing vapor bubble passes through a small thin film area, where the liquid-vapor interface meets the solid wall. In this micro region (Stephan and Hammer 1994), the heat flux can be up to 100 times higher than mean heat flux through the system (Dhir 2001). The thickness of the liquid film in the contact line region is very thin ($O(1 \mu\text{m})$) and its thermal resistance is very small. This gives rise to a high evaporation rate at this region. A gradient of capillary pressure due to interfacial curvature change provides a transverse flow from the liquid bulk into the micro region. Experimental studies of pool boiling performed in microgravity showed a temperature drop in near the 3-phase contact line (liquid-vapor-solid junction) caused by a significant evaporation rate in the contact line region (Wagner et al. 2006; Schweizer 2010; Fischer et al. 2012; Sodtke et al. 2006). For specific parameters and fast growing bubbles an additional micro layer with a thickness of $O(10 \mu\text{m})$ and length of $O(1 \text{ mm})$ can be formed. Exemplary measurements with water as experimental fluid at atmospheric pressure can be found in Koffman and Plesset (1983), Kim and Buongiorno (2011), Utaka et al. (2018) and Jung and Kim (2018). Sielaff (Sielaff 2014) observed the same behavior for low pressures also with FC-72 as the experimental fluid. Schweikert et al. (2019) investigated the influence of dewetting speed, heating power and overheating on the formation of this thin film by means of a dedicated dewetting experiment and determined a threshold value for the formation of this thin film.

Investigations of boiling process under reduced gravity have been performed using various platforms such as drop tower, sounding rockets, parabolic flights and space missions. One of the experiments supported by the European Space Agency (ESA) within the utilization program of the International Space Station (ISS) is the multiscale boiling project (Tóth et al. 2012). This project aims at studying the fundamentals of boiling by analyzing the nucleation of a single vapor bubble on an isolated nucleation site, its growth and detachment. Unique features

of the multiscale boiling project are the possibility to observe and measure local transport phenomena, and to assess the effect of an external electric field as well as the influence of a shear flow on the behavior of a single bubble. The experiments are conducted in the Fluid Science Laboratory (FSL) of the Columbus module of the ISS.

In preparation of the multiscale boiling project and in order to determine a promising operational parameter range for the experimental components developed at the Institute of Technical Thermodynamics in Darmstadt, similar boiling experiments have been conducted in a microgravity environment in the framework of the ESA 70th parabolic flight campaign in October 2018. Data of the experiments were collected during three subsequent flights with 31 parabolas each. Each manoeuvre starts with flying at a steady horizontal altitude, with an approximate speed of 810 km/h. In this phase, the gravity level is approximately 1 g. At a set point, the pilot starts pulling up the nose of the aircraft resulting in a gravity level of 1.5 to 1.8g. This phase lasts for about 20s. With an angle of around 47 degrees relative to horizontal level, the engine thrust is reduced to a minimum required to overcome the air drag. At this point the aircraft experiences weightlessness, as it follows a free-fall ballistic trajectory lasting for approximately 20s. At the end of this zero-gravity period, the aircraft must pull out of the parabolic arc giving rise to a 20s hypergravity phase at a level of 1.8g. Finally, the aircraft flies a steady horizontal path at 1g before the procedure starts again. A parabola with its different phases is illustrated in Fig. 1.

In this work, the focus is put on the analysis of the results obtained for pool boiling, in the absence of any external forces. A detailed description of the experimental setup, the measurement systems and procedures is given in Section “[Experimental Setup and Measurement Principles](#)”. In this section, all main parts of the experimental setup are addressed, although some of them are not employed for

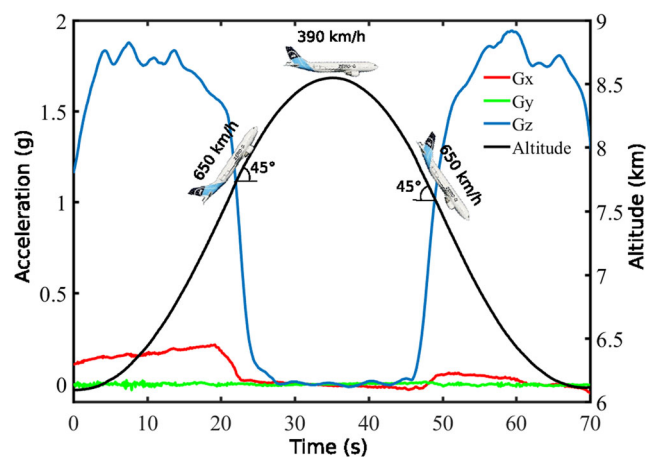


Fig. 1 Measured flight parameters during one parabola, announced by Novespace

obtaining the results in this work. Finally, the experimental findings are presented and discussed in Section “Results and Discussion”.

Experimental Setup and Measurement Principles

The concept of the experimental setup used in this work is adopted from the multiscale boiling project. However, some modifications have to be carried out to adapt the setup for the specific conditions during parabolic flights. A major difference compared to the multiscale boiling project on the ISS is the repetitive change in the gravity level. The core of the experimental setup is the boiling cell with a heating element. The heater assembly is composed of a crystal substrate with a sputtered chromium nitride and chromium heating layer on top and an artificial nucleation site in the center. The boiling process takes place at this substrate heater. It is initiated by locally superheating the area around the nucleation site using a focused laser beam. The temperature distribution on top of the substrate heater surface is measured from the back side by means of high speed infrared (IR) thermography, while the bubble shapes are observed employing a high speed black-and-white (BW) camera from the side. The temperature inside the bubble and inside the thermal boundary layer near the liquid-vapor interface is measured by a rack of four micro thermocouples. Two systems are used to apply forces on the vapor bubbles: (i) an electric field applied by an electrode positioned above the substrate heater surface and (ii) a shear flow in the bulk liquid created by a fluid circuit loop. The experimental setup is schematically shown in Fig. 2.

For the parabolic flight campaign the experimental setup with the measurement and control systems as well as the electronic devices are placed in two racks, each fixed on the aircraft floor. Rack no. 1 contains the boiling cell, cameras, laser and temperature control, while in rack no. 2

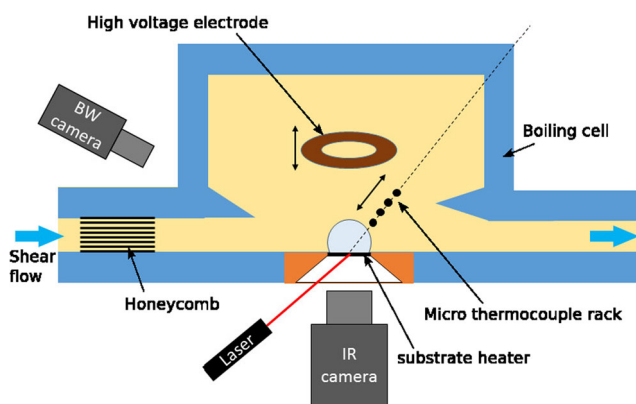


Fig. 2 Schematic illustration of the boiling cell

measurement devices and power supplies are installed. In the following subsections, the experimental setup placed in the rack no. 1 is explained in detail.

Boiling Cell

The heart of the experimental setup is the boiling cell made of stainless steel with external dimensions of 117 x 90 x 91 mm. The boiling cell has three main cut-outs for slide-in modules, one for the insertion of heater assembly, one for the insertion of the high-voltage electrode, and one for the insertion of the micro thermocouple rack. In order to measure the temperature of the cell, thermocouples of type K are used at different positions. The CAD model of the boiling cell and its modules are shown in Fig. 3a and b.

On the upper side of the cell there is a borehole for connections to a filling nozzle, a pressure sensor, and a volume compensation tank. A narrow passage allows vapor to pass from the test cell into a vapor trap during gravitational flight phases. This is necessary to prevent vapor accumulation in the test cell and vapor reflow during residual negative acceleration during the zero-gravitational flight phases.

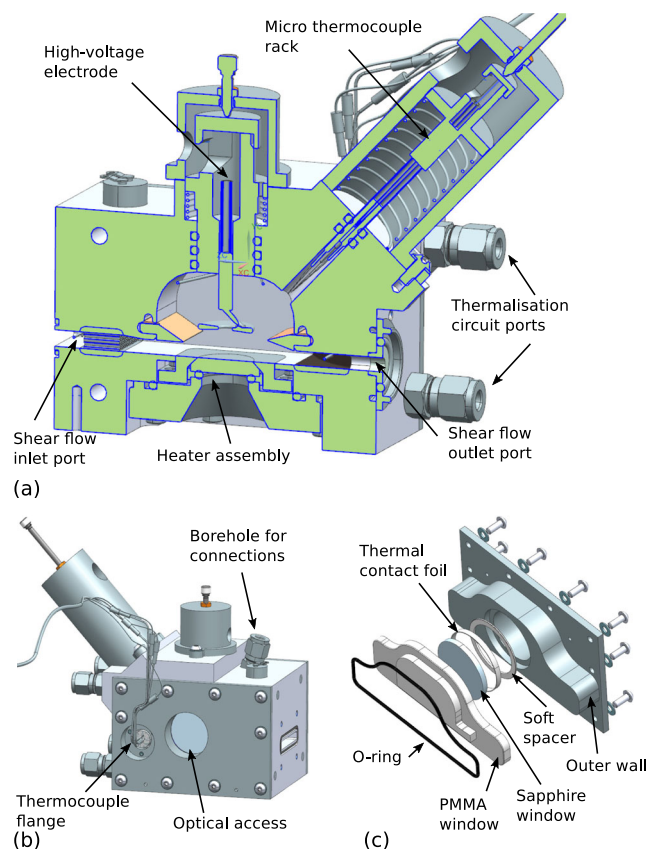


Fig. 3 a Cross-section of the schematic illustration of the boiling cell and its modules b CAD model of the boiling cell c Exploded view of the double window

The hydrodynamic behavior of the bubble is observed through a window in a side wall of the boiling cell using a BW camera (model MotionXtra N4, IDT Vision) with diffuse backlight illumination through a window on the opposite side. The camera captures images with the rate of 500 frames per second. Each window consists of a double layer assembly, illustrated in Fig. 3c, with a 20 mm thick polymethylmetacrylate (PMMA) plate and a 3.17 mm thick circular sapphire glass.

The heater assembly is installed at the bottom of the test cell. The main element of the heater assembly is a circular barium fluoride (BaF₂) single crystal (manufactured by Korth Kristalle GmbH) with a chamfer of 45°. It is optically transparent from the ultraviolet wavelength 150nm to infrared wavelength 15 μm . This allows for IR thermography from underneath the test cell. A L-shaped artificial nucleation site is lasered into the center of the crystal from the top. The diameter of the nucleation site at the surface of the crystal is 30 μm , while its depth and side length are 200 μm and 100 μm , respectively. It should be noted that the geometry of the cavity should provide a stable nucleation by leaving a residual amount of vapor after a bubble has left the area of the cavity. Based on this reason, a L-shape for the nucleation site has been selected, which is shown schematically in the inset of Fig. 4.

The crystal with the nucleation site is then coated with two layers using physical vapor deposition (PVD). The first layer is a high emissive chromium nitride layer to enable the IR thermography. The second layer is a pure chromium layer which acts as a Joule heater. Details of the manufacturing processes are as follows.

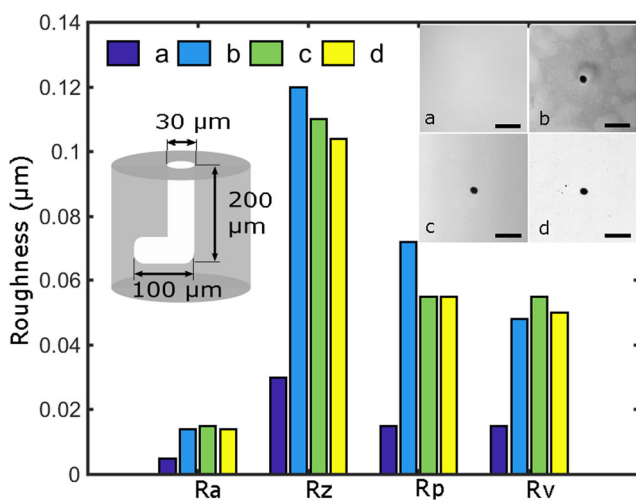


Fig. 4 Roughness parameters Ra, Rz, Rp and Rv of an exemplary crystal for **a** before usage, **b** after manufacturing of nucleation site, **c** after cleaning and polishing and **d** after PVD sputtering. In the insets at the right side, confocal microscopy images of the crystal surface (taken by Leica DCM 3D) are shown. The scale bars correspond to 100 μm . In the inset at the left side, nucleation site is schematically illustrated

The nucleation site is brought into the crystal by applying ultra short laser pulses with a central wavelength of 800nm (Laser Zentrum Hannover e.V.). The crystal is transparent for this wavelength. However, due to the multiphoton effect it can be attacked at the laser focal point. The minimum amount of energy required for erosion in volume is much higher compared to the one at surface. For this reason and based on the focusing of the laser, the distance of the cross cut of the L shape to the surface has to be sufficiently large, in order to prevent surface damage. Therefore, the depth of cavity is set to 200 μm . For removing the barium fluoride particles, the crystal is situated upside down on an O-ring in a container of water, while only the lower surface of the crystal is in contact with water. Owing to the high energy of the laser, bubbles are induced in water, which support the particle removal from the treated crystal. The manufacturing process has been also tested in isopropanol, which did not exhibit satisfactory results. The entire laser process takes almost 5 minutes. Afterwards, the crystal is cleaned with compressed air.

Since the barium fluoride is soluble in water, a pattern can be observed at the crystal's surface, which is a combination of roughening, deposits and particles. As the PVD process is highly sensitive to the surface quality, treatment of the surface prior to the coating is of great importance to make sure that the desired coating characteristics can be achieved. Note that the surface defects or particles can influence the density and micro texture of the coating. Therefore, a combination of cleaning with acetone, air blowing and polishing was employed for each crystal. The surface roughness measured for the entire process, from the bare crystal before manufacturing the nucleation site to the sputtered surface is depicted in Fig. 4.

The coating was synthesised with an industrial scale deposition unit type Cemecon CC800/9 HPPMS. As sputter method, a combination of HiPIMS (High Power Impulse Magnetron Sputtering) and DCMS (Direct current Magnetron Sputtering) was used. In the first step a chromium nitride (CrN) layer with the thickness of 400 nm is sputtered on the barium fluoride crystal. An aluminum mask has been used to define the geometry of the coating. The coating has to be dense, thin and manifest high emissivity to support the thermography. Subsequently, the chromium (Cr) used as the heating layer is sputtered on the chromium nitride coating. This layer has also a thickness of 400nm. The thickness was chosen with the aim of having a layer as stable as possible which exhibits a high electrical resistance at the same time. For use on the ISS, an electrical resistance of at least 10 Ohm had to be guaranteed in order to be compatible with the electrical components. The sputtered glasses exhibit different electrical resistances ranging from 10 to 16Ohm. The resistance of the heater used in this work is 11.5Ohm at 20 °C. In order to measure the

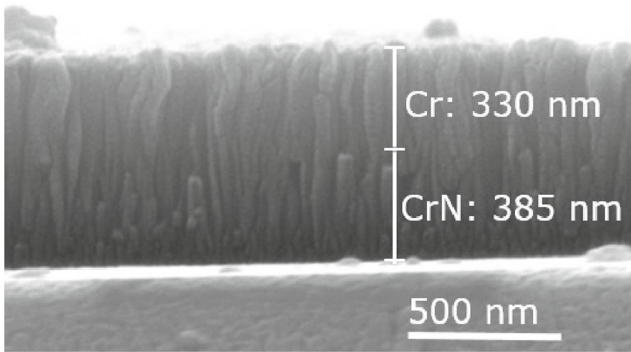


Fig. 5 Scanning electron microscopy image of high emissive chromium nitride layer and chromium heater layer on top

exact thickness of each layer, the sputtered crystal has to be broken allowing for observation of the cross section of the layers (Fig. 5).

To find out the thickness influence on the emissivity character of the coatings, an IR camera (VarioCAM, infratec) has been used to measure the emissivity indirectly at different thicknesses and temperatures. The measurements have been conducted five times for five different temperatures ranging from 30°C to 70°C. The IR camera has been calibrated in the same temperature range using a thermal paint (HE6/HE23, Rolls-Royce) with the known emissivity of 0.97. The surface temperature of the coating is adjusted using a heating plate and measured with a calibrated thermocouple. It is found that the emissivity of the chromium nitride layer for the thicknesses ranging from 300nm to 700nm is almost constant. However, the combination of the chromium layer on the chromium nitride coating exhibits much higher emissivity character. This behavior is shown in Fig. 6. In this case, the incoming radiation is partly transmitted through the chromium nitride coating and partly reflected or absorbed by the chromium layer. As a result, the thickness reduction due to resistance optimisation does

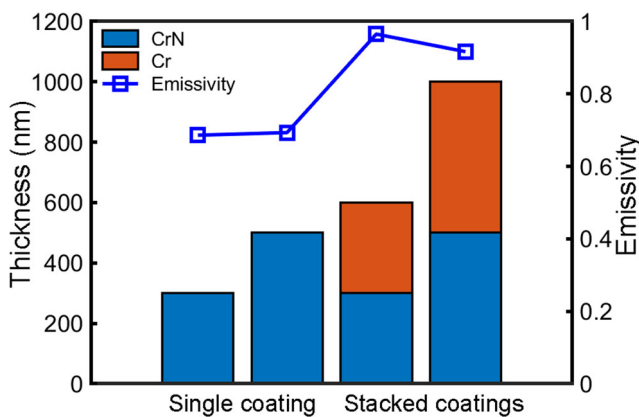


Fig. 6 Emissivity of single coating of CrN as well as stacked coatings of Cr over CrN at 70°C as a function of thickness

not lead to any significant affect on the emissivity of the coating. Note that the maximum allowable thickness of the chromium coating is 400nm, since the electrical resistance of the coating should be at least 100Ohm.

The geometry of the heating layer is designed in such a way that in the centre of the heater (in the scientifically relevant area for the measurements) the heating power is as homogeneous as possible, but at the same time the possibility of parasitic boiling in the remaining area and at the connections is reduced. Therefore, the width of the layer is reduced towards the center of the heater having a constant width in the vicinity of the cavity. The geometry of the layer is shown in Fig. 7. The chromium layer as heating element is electrically contacted using two copper wires on the each side of the glass. In order to provide a contact with possibly small electrical resistance and an increased mechanical stability, the sides of the substrate heater are sputtered with 4µm copper layer. Then the wires are connected using electrically conductive glue (Elecolit 325, Bürklin) to the sputtered copper layer. Four feedthroughs integrated in the

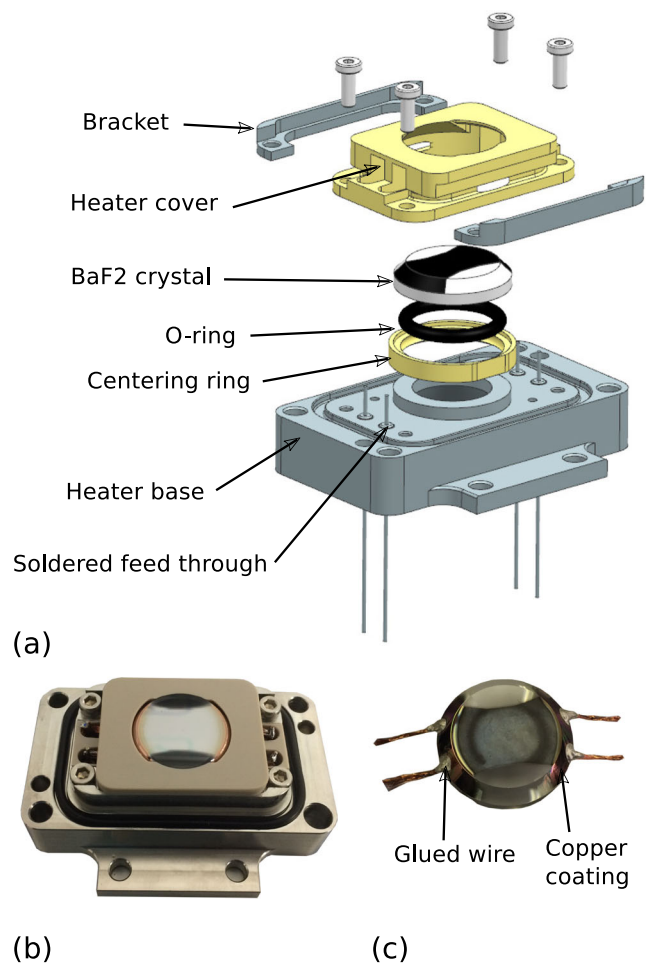


Fig. 7 a Exploded view of the heater assembly b Heater assembly c Substrate heater with copper coating on the sides

heater base are used to connect the substrate heater to the power source. The substrate heater with connected wires are shown in Fig. 7c.

The substrate heater is assembled by a Polyetheretherketon (PEEK) cover pressing the substrate heater and the O-ring underneath into a centering ring providing the necessary leak tightness for the heater assembly. The heater base is screwed finally into the boiling cell and sealed with an O-ring. The heater assembly is shown in Fig. 7a and b.

The necessary superheat for bubble initiation at the artificial cavity on the substrate heater is provided by a laser beam at a wavelength of 404nm. The beam is produced by a laser diode (L404P400M, Thorlabs) delivering an output power up to 400mW. After leaving the diode, the laser beam is collimated and then focused using a lens with the focal length of 200mm. The position of the lens is adjusted in such a way that the focused laser beam meets exactly the artificial cavity on the substrate heater. In order to control the duration of the laser pulse, a shutter (type SH05, Thorlabs) is installed directly after the diode. In the experiments, the laser pulse duration is set to 300ms. This long duration has been selected to study the influence of the laser energy on the growth of bubbles.

In order to study the influence of an electrical field on vapor bubbles, a high-voltage system has been installed in the experimental setup. It consists of a high-voltage electrode made of copper, the feedthrough to the electrode and a high-voltage power supply (HP series, Applied Kilovolts Ltd) with dedicated electronics. The high-voltage electrode is produced by selective laser melting and has a washer-like shape with an outer diameter of 20 mm, an inner diameter of 5 mm and a thickness of 1mm. It is placed centrally above the substrate heater in the boiling cell, while its circular plane is parallel to the heater surface. The high-voltage electrical system is operated with DC voltage up to 15kV. The electrode is connected to the power supply using a shielded bushing for electrical isolation from the housing. A screw with fine thread on the upper side of the construction allows the fine height adjustment of the electrode. The lowest position of the screw corresponds to a distance of 6 mm to the surface of the substrate heater.

The IR thermography is performed with a high-speed camera (model X6901sc, FLIR Systems), recording 4000 images at a resolution of 640 x 512 pixels and rate of up to 1000 frames per second. A calibration of the camera is performed like presented in Sielaff (2014) and Schweizer (2010).

The micro thermocouple rack (MTCR) is composed of four micro thermocouples of type K with a sheath diameter of 0.5mm, whose tips are positioned with a certain offset compare to each other. The measuring tip has a diameter of approximately 100 μ m. Each thermocouple

has its individual cold junction in a form of a copper block located in a temperature calibrator device (CTD9100-ZERO, WIKA). According to the manufacturer, the temperature distribution in the block is assumed to be homogeneous, while the accuracy of the calibrator is 0.05K at a temperature of 0°C.

Fluid Circuit System

To generate a shear flow in the boiling cell, a fluid circuit with working medium of FC-72 is designed. In this work, all components of the FC-72 circuit are named with index 1. The flow diagram is shown in black lines in Fig. 8. The fluid is pumped using a hermetically sealed gear pump P1 (model FG304XPS24N, Fluid-o-Tech) driven by a magnetic coupling. The pump can provide volume flow rates of up to 500ml/min. After the pump, a Coriolis flow sensor (model FD-SS2A, Keyence) is installed, which can measure the flow rates up to 2000ml/min. Before the boiling cell BC, a heating cord H1 (type HS/030, Hillesheim GmbH) is used to heat the fluid. The heating cord has a length of 3m and power of 350W.

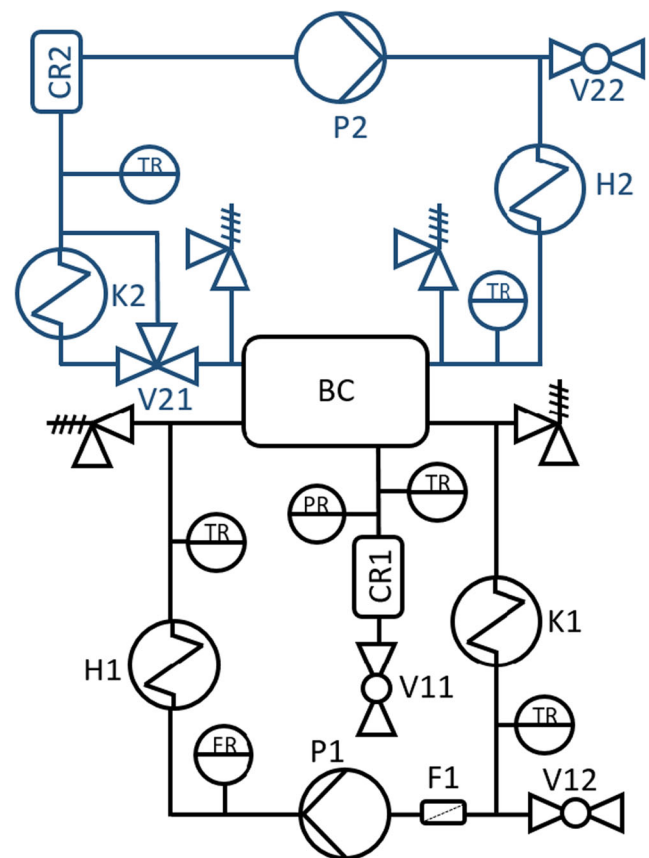


Fig. 8 Schematic illustration of the fluid circuit system. The black lines show the FC-72 circuit used for applying shear stress on the nucleated bubbles, while the blue lines illustrate the water circuit for thermalization of the boiling cell.

For applying a shear flow on the vapor bubbles, an inlet and outlet port have been foreseen in the boiling cell. In the direction of the fluid flow, the interior of the cell is divided into the following parts: flow inlet, honeycomb structure and flow straightener for making an one dimensional laminar flow, heated area and central space for bubble generation, flow collector and flow outlet. Before the inlet port, there is an adapter to expand the flow from a circular pipe to a rectangular cross-section.

After the boiling cell, the fluid flows through a cold plate K1 (CP15G01, Lytron) with an outside heat sink (LA32, Fischer Elektronik). A filter F1 collects potential particles in the fluid circuit and ensures a safe operation of the pump. The pressure in the system is measured above the boiling cell in the vapor phase. As pressure sensor serves an absolute pressure transmitter (model PAA-23, Keller AG) with zero point at vacuum. The sensor can be used for a pressure range of up to 2bar and has an accuracy of ± 4 mbar.

The expansion tank CR1 is designed for the thermal expansion of the fluid and installed after the pressure sensor. Two overpressure valves are used before and after the boiling cell opening at a pressure of 3bar. The temperature in the fluid circuit is measured using thermocouples type K at three different locations: after the heater H1, after the boiling cell BC and after the Cooler K1. The leakage rate of the working fluid circuit is 10^{-4} mbar l /s and filled with degassed FC-72.

In order to achieve a homogeneous temperature distribution as well as a rapid thermalization of the boiling cell, a second fluid circuit with working medium of water has been used. For this purpose, two U-shaped channels are inserted into the block of the boiling cell. The flow diagram of the water circuit is shown in blue lines in Fig. 8. All components of the water circuit are named with index 2. The pump P2 (DDC, Laing) is used to circulate the water, while a heating cartridge H2 is employed to heat the water before flowing into the boiling cell. In order to cool down the flow, a cold plate K2 (CP12G01, Lytron) connected to a heat sink on the outside (LA32, Fischer Elektronik) is installed after the boiling cell. For a rapid heating of the boiling cell, the cold plate K2 can be bypassed using the three-way valve V21. A compensation reservoir CR2 is placed shortly before the pump. Two overpressure valves are installed before and after the boiling cell which are set to a pressure of 3 bar. The temperature in the water circuit is measured after the heater and cooler by means of thermocouples.

Measurement Procedure

The experimental setup is controlled and monitored by the LabVIEW software reading the low-speed data (e.g. cell temperatures) and setting the experimental parameters. The high-speed data (BW and IR camera) are recorded

on a corresponding computer each. The synchronisation is performed by individual trigger signals to measurement and control devices. For a measurement during the 0g phase the substrate heater assembly is switched on with the set current provided by a power supply. In the last 1000ms of the preheating time, the light source of the BW camera is switched on, whereas the BW and IR cameras are triggered 500ms later. The laser shutter is opened at the end of the preheating time leading to activation of the nucleation site by the laser beam. All measurement data are recorded for a period of 5000ms. This process is shown in Fig. 9.

Heat Flux Calculation

The heat flux at the top of the heater surface, i.e. at the solid-fluid interface, has been calculated using the temperature fields captured by IR thermography. To this end, an OpenFOAM code has been developed based on the finite volume method, which discretizes the entire heater substrate into finite volumes and solves the energy equation for each of them. The numerical grid has a rectangular shape, while its top surface has the same dimension as the captured IR images. Every cell at the surface corresponds to a pixel in the IR image, while the cell size is exactly equal to the pixel size. As the boundary condition at the top surface, the temperature field captured by IR camera is applied in every time step. In order to match the simulation with the measurements, time step of the simulation is taken from the measurement sequence. For the sake of simplicity, the other five surfaces are considered to be adiabatic. As the initial condition, the average temperature calculated from the first IR image is applied for the temperature field in the entire domain. In the transient simulation, the three-dimensional heat conduction equation

$$\frac{\partial T}{\partial t} = \nabla \cdot (\alpha \nabla T) \quad (1)$$

is solved for every time step.

Here, T stands for the temperature, while α denotes the thermal diffusivity of the substrate material. In the next step, the heat transfer orthogonal to the top surface is determined by applying the Fourier's law. Here, the imposed temperature field on the top surface and the temperature field within the body resulted from the numerical simulation are used for calculating the temperature gradient in normal direction.

The output of the simulation is the local heat flux at the interface of barium fluoride glass and the chromium nitride layer. Since the lateral heat conduction within the heating layer can be neglected, the heat flux at the solid-fluid interface can be calculated by adding the heat source term (Joule heating) to the outcome of simulation. The resulting heat flux fields have a same temporal and spatial resolution as those for the temperature fields. In this special

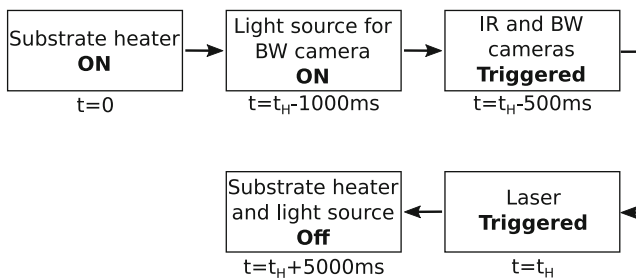


Fig. 9 Block diagram showing the execution process for a measurement sequence

case the additional heat flux provided by the laser is not accounted for in the calculation, as it is part the evaluation.

Results and Discussion

The development of a bubble captured by BW camera from the instance of nucleating using laser is shown in Fig. 10. Note that in this work, at the instance of shooting the laser beam, the time is set to zero. The evolution of the bubble taken by IR camera is presented in Fig. 11. Four diagrams have been displayed for each stage of evolution. In the upper row, the temperature field on the backside of the chromium layer captured by IR thermography is displayed in the left graph, while the local heat flux at the heater-fluid interface, evaluated as described before, is depicted in the right graph. The distances on the X and Y axis are illustrated in millimeter. In the lower row, the profile of the local heat flux and temperature along the lines depicted in the upper graphs are shown in two separate plots. Here, two different colors are used for two positions. The red line corresponds to the $x = 2.25\text{mm}$, whereas the blue line is located at $x = 3.5\text{mm}$. These positions have been chosen for comparing the influence of the laser beam at different distances. The temperature of the blue line is shown on the left y-axis, while the temperature of the red line is depicted on the right one. The artificial nucleation site is located approximately at $x = 4\text{mm}$, where the focused laser beam is shot. In this experiment, the pressure in the boiling cell is 0.8bar , the laser power is $P_L = 400\text{mW}$, the heater power density is $P_H = 1.36\text{W/cm}^2$ and the preheating time is $t_H = 10\text{s}$. Before shooting the laser, the average surface temperature is $64.3\text{ }^\circ\text{C}$. By considering

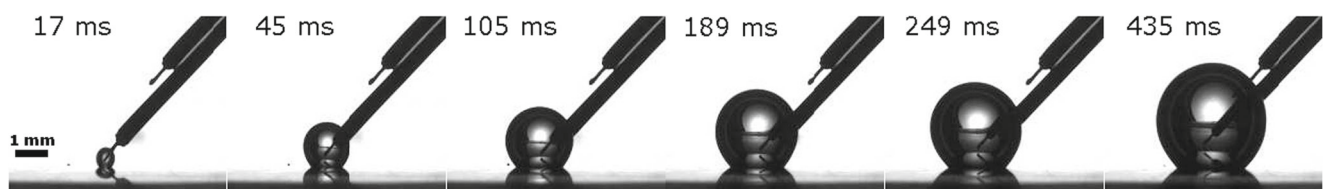


Fig. 10 Nucleation and growth of a bubble

the saturation temperature of $T_{sat} = 50.4\text{ }^\circ\text{C}$, the liquid near to the heater surface is $13.9\text{ }^\circ\text{C}$ super heated. Since the chromium layer sputtered on the glass exhibits an extremely flat surface, the nucleation does not occur spontaneously and requires an initial excitement. This can be observed in the graphs of local heat flux, as the fluctuation of the heat flux far from the nucleation site is extremely small.

In the first stage of Fig. 11, a nucleated bubble at 13ms after the laser shooting is displayed. The bright point in the temperature field is caused by the laser inducing a calculated negative heat flux. As mentioned before, the heat flux of the laser is not considered in the calculations. This leads to the negative values shown. In this case, the influence of the laser can be compared with the overall heat flux on the surface. It should be noted that the direction of the heat flux is assumed out of the heater surface. This means that the extracted heat flux from the surface is considered as positive, while the imported heat flux to the surface is negative. It can be clearly observed that by nucleation of the bubble, the heat flux on the blue line increases considerably close to the position of the nucleation site. Next to the extraction of the FC-72 latent heat from the heater surface, the high heat flux can be attributed to the transportation of a part of the laser energy to the liquid phase. In case of only extracting of the latent heat from the surface, the surface should be cooled down, while here an increase of about $4\text{ }^\circ\text{C}$ can be seen in the temperature profile which is induced by laser energy. With growing bubble size and formation of the 3-phase contact line, the evaporation in its proximity leads to a local cold ring on the heater surface with temperature drop of $0.2\text{ }^\circ\text{C}$ to $0.3\text{ }^\circ\text{C}$ compared to adjacent points on the heater surface. This effect is supported in the heat flux evaluation by formation of a ring with heat fluxes ranging from 5500W/m^2 to 7400W/m^2 above the mean value. Note that in zero-gravity environment, the heat transfer occurs only through conduction and no convection takes place. Due to the low thermal conductivity of the FC-72 vapor ($k = 8.3 \times 10^{-3}\text{ W/(mK)}$) the most of the laser energy is transferred to the barium fluoride glass. In order to calculate the heat transfer caused by the laser in a precise manner, a simulation has been conducted utilizing COMSOL 5.3. Here, the heat generated by the laser has been considered as a heat source which is placed between barium fluoride glass and FC-72. The simulation showed that based on the

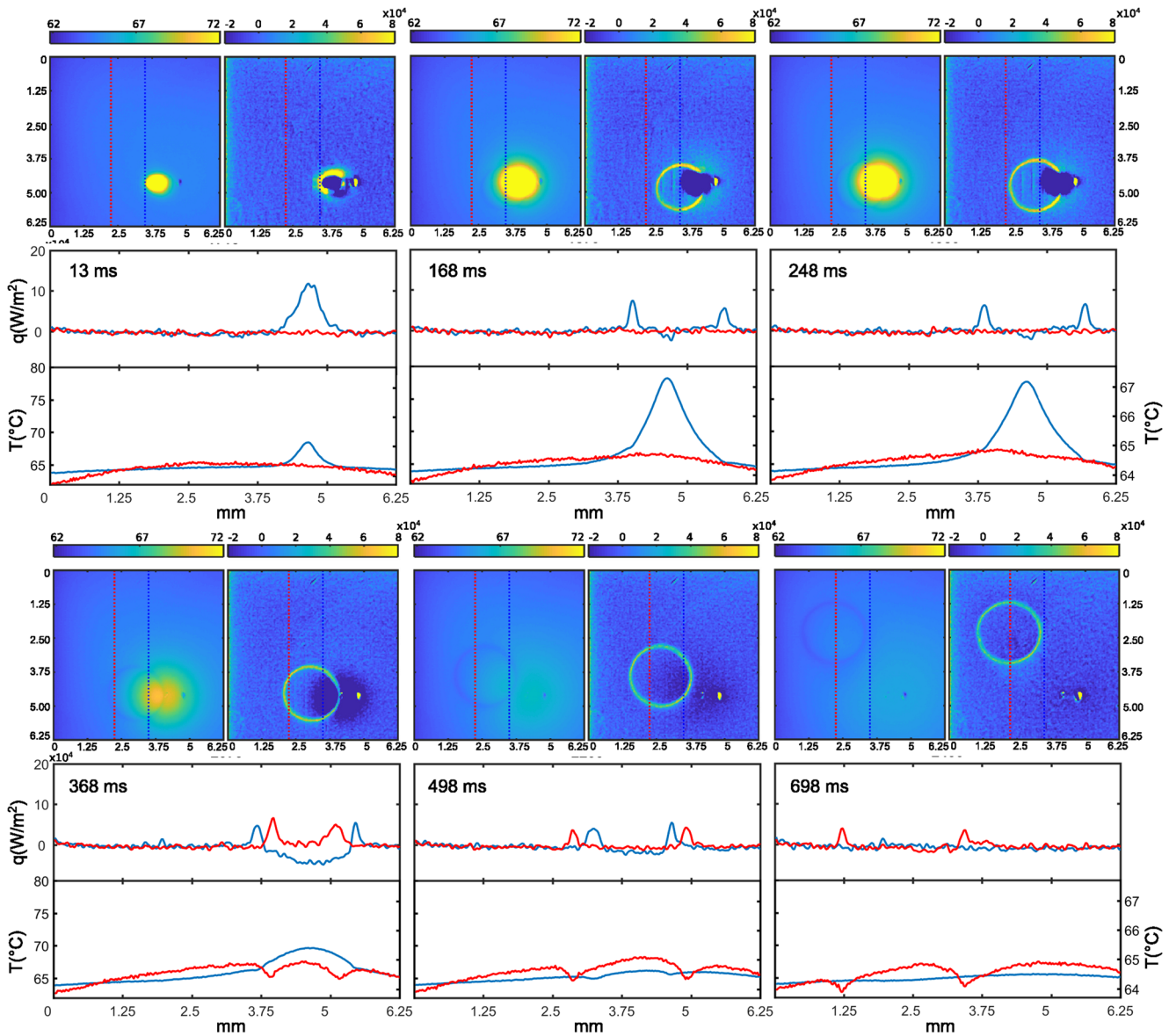


Fig. 11 Nucleation and evolution of a vapor bubble. Here, the preheating time is $t_H = 10s$, the laser power is $P_L = 400mW$ and the heater power is $P_H = 1.36W/cm^2$. For the temperature profiles, the left axis corresponds to the blue curve, while the right one is for the red curve.

poor thermal conductivity of the FC-72 vapor compared to the one of the barium fluoride, only less than 3% of the laser energy is transferred to the bubble, while more than 97% of that is conducted to the glass. The thermal conductivity of the barium fluoride is $10.9W/(mK)$ at $32^\circ C$.

At 368ms, the bubble reaches the position of the red line. The temperature profile along the red line exhibits two minimums corresponding to the intersection positions with the 3-phase contact line. This is verified by two peaks in the corresponding heat flux profile. Here, no influence of the laser can be observed, as the temperature profile is pretty uniform. With further increasing of time, the bubble starts moving so that at 698ms the blue line has no intersection with the 3-phase contact line. The temperature maximum on

the blue line decreases, as the surface is cooled down in the absence of the laser.

The mean heat flux and wall temperature as a function of time are shown in the left graph in Fig. 12. As mentioned before, at the instance of shooting the laser, the time is set to zero. At this moment, it can be observed that the calculated mean heat flux on the wall becomes negative. The negative value of the mean heat flux supports the former mentioned analysis that the largest portion of the laser energy is transported by conduction to the substrate heater. In the mean temperature profile, the laser induces a sharp maximum. As the laser is switched off, the mean temperature starts decreasing whereas the mean heat flux becomes positive again. Since during the experiment

the heater is on and the surface gets warm, the mean temperature of the surface develops a minimum at 600ms and rises again. As time goes on, the nucleated bubble moves out of the field of view of the IR camera (at 900s) resulting in decrease of the mean heat flux.

Right graph of Fig. 12 shows the diameter of the bubbles as a function of time and preheating time. In order to measure the bubble diameter, a MATLAB code has been developed to post process the BW images and detect the edge of the bubbles. As mentioned before, due to the lack of buoyancy force the bubble departure diameter in reduced gravity is larger than the one in 1-g condition. As the bubbles grow to larger diameters, the moving velocity of the 3-phase contact line decreases. This behavior can be observed clearly in the graph, since the slope of the curves decreases with increasing of time. The low moving velocity of the contact line allows for measurement of the local temperature drop at micro region. In this graph, it is also obvious that with increasing the preheating time, the diameter of the bubble increases as well. This behavior can be attributed to the temperature of the chromium layer at the instance of nucleating a bubble. With increasing the preheating time, the temperature of the chromium layer increases. For the case of $t_H = 5s$, the surface temperature before nucleating a bubble is $T_W = 60.95^\circ\text{C}$, while this value increases to $T_W = 69.5^\circ\text{C}$ for the preheating time of $t_H = 30s$. Note that these results are obtained for the heater power of $P_H = 1.36\text{W}/\text{cm}^2$ and the laser power of $P_L=400\text{mW}$, while the saturation temperature is $T_s = 50.4^\circ\text{C}$. Since the microgravity phase in a parabola lasts about 22s, for setting the preheating time of $t_H = 30s$ the heater has to be turned on during the hypergravity phase. This can affect the temperature of the heater surface and reduce it compared to

the one in microgravity phase, as in the hypergravity phase convection mode of heat transfer takes place.

The parabolas during the flight are accompanied most of the time with quasi steady residual acceleration defined as G-jitter, which slightly changes the orientation and magnitude of a body force in testing environment. These accelerations are caused usually by crew activities or equipment operation as well as by aerodynamic and aeromechanical forces on the airplane itself. The fluctuations observed in the diameter evolution of the bubbles in the right graph of Fig. 12 are caused by G-jitter, since the body force acting on the bubbles is altered periodically.

Note that no major change in the diameter of the bubbles can be observed, as the laser pulse duration of 300ms is over. This shows that the laser energy has less influence on the bubble growth rate, because it is hardly transferred to the bubble. This result supports the presumed mechanism that the laser energy is mainly transferred to the barium fluoride glass and only a small part of it is transferred to the bubble.

Conclusions

In preparation of the multiscale boiling project, a boiling experiment in zero gravity within the course of utilization of the International Space Station (ISS), an experimental setup is constructed to study the nucleate boiling and determine the operational parameters for the experimental components. The experimental setup is equipped with two systems to apply forces on the bubbles: an electric field using a washer-shaped electrode and shear flow created by a fluid circuit loop. However, in this work the concentration is put on the pool boiling without any external forces. As

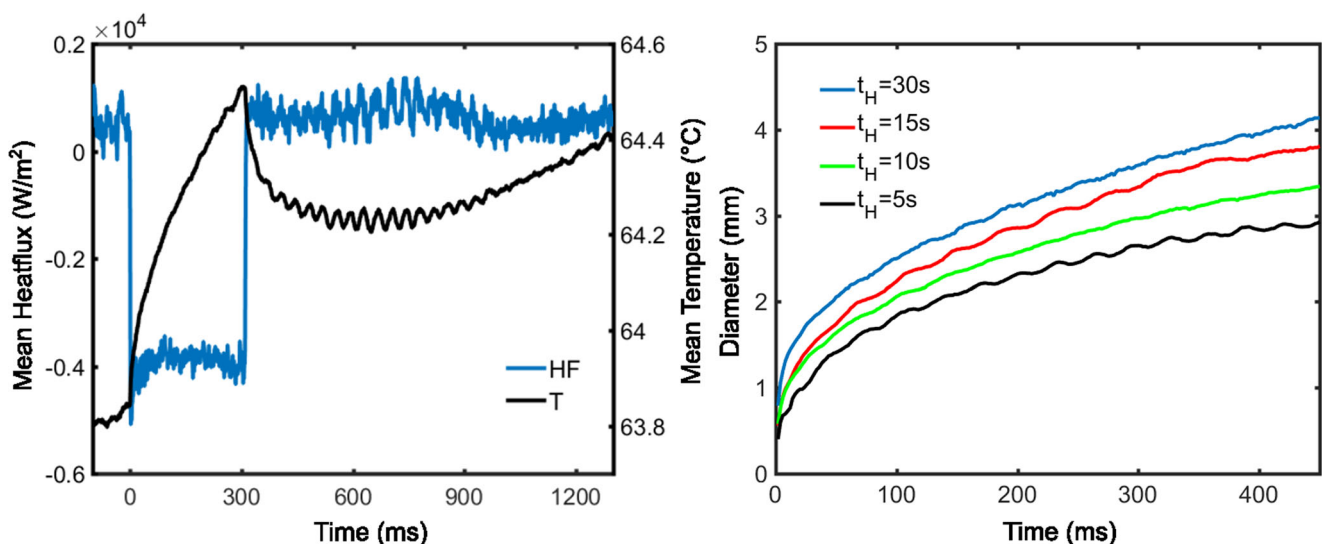


Fig. 12 Left: mean heat flux and temperature of the heater surface over the area of 8.75x8.75mm. Right: diameter of the bubbles as a function of time and preheating time t_H

the heater, a barium fluoride glass sputtered with chromium layer on the top of a coated chromium nitride layer is employed, which is electrically connected to a power supply. In order to nucleate a bubble, an artificial cavity is manufactured in the center of the glass, which is activated by a laser. The temperature distribution on the back side of the sputtered layers has been measured using infrared thermography, while the evolution of the bubbles is captured by a high speed black-and-white camera. An in-house OpenFOAM code has been used to calculate the heat flux on the heater surface based on the temperature fields measured by the infrared camera. In order to test the operational capacity of the designed heater and also study the influence of the laser energy on the bubbles, the laser pulse duration is set to 300ms, which is extremely long. Furthermore, the power density of the heater is set to $P_H = 1.36\text{W/cm}^2$, which is higher than the maximum power required for the multiscale project. It has been shown that the laser energy facilitates the nucleation of the bubble, as it increases the temperature at the artificial cavity. However, after the formation of the bubble and appearing of 3-phase contact line, the most of the laser energy is transferred to the barium fluoride glass. A conducted numerical simulation has supported this mechanism and showed that more than 97% of the laser energy is conducted to the glass, while only less than 3% of it is transferred to the FC-72 vapor. Based on this reason, it is shown that the growth rate of the bubbles is almost independent of the laser pulse duration, as the most of the laser energy is transferred to the glass through conduction. Considering the time between two different experiments (and consequently laser shots) of approximately 5 minutes in parabolic flight and 30 minutes on the board of the ISS, it can be concluded that no significant influence of the laser shot on the bubble dynamics is expected.

The effect of preheating time, defined as the time delay between turning on the heater and shooting the laser beam, on the diameter of the nucleated bubbles has been studied. It is shown that by increasing the preheating time, the surface temperature at the instance of nucleation increases giving rise to larger growth rate of the bubbles.

Acknowledgments We would like to thank the German Aerospace Center (DLR) for the financial support in the framework of the “Vapor project”, grant no. 50WM1654. We would also like to express our gratitude to the European Space Agency (ESA) and Novespace for providing the possibility to perform the experiments in microgravity in the course of the 70th ESA Parabolic Flight Campaign. We further would like to acknowledge the support by the German Research Foundation (DFG) within the Collaborative Research Center 1194 “Interaction between Transport and Wetting Processes”, project no. A01 and C02. We are also immensely grateful to Airbus Defence and Space for providing the RUBI breadboard cell. Additionally, we would like to thank the German Research Foundation (DFG) for funding the project “Verification and valuation of long term behavior and resistance of thin coatings under electrothermic and cavitation erosion stress within nucleate boiling”, grant no. SCHE 1423/5-1.

References

- Cole, R.: Bubble frequencies and departure volumes at subatmospheric pressures. *AIChE J* **13**(4), 779–783 (1967)
- Cole, R., Rohsenow, W.: Correlation of bubble departure diameters for boiling of saturated liquids, vol. 65, pp. 211–213 (1969)
- Dhir, V.K.: Numerical simulations of pool-boiling heat transfer. *AIChE J* **47**(4), 813–834 (2001)
- Fischer, S., Herbert, S., Sielaff, A., Slomski, E.M., Stephan, P., Oechsner, M.: Experimental investigation of nucleate boiling on a thermal capacitive heater under variable gravity conditions. *Microgravity Sci. Technol.* **24**(3), 139–146 (2012)
- Fritz, W.: Berechnung des maximalvolumen von dampfblasen. *Physik Zeitschr* **36**, 379–384 (1935)
- Jung, S., Kim, H.: Hydrodynamic formation of a microlayer underneath a boiling bubble. *Int. J. Heat and Mass Transf.* **120**, 1229–1240 (2018). <https://doi.org/10.1016/j.ijheatmasstransfer.2017.12.098>
- Kim, H., Buongiorno, J.: Detection of liquid–vapor–solid triple contact line in two-phase heat transfer phenomena using high-speed infrared thermometry. *Int. J. Multiphase Flow* **37**(2), 166–172 (2011). <https://doi.org/10.1016/j.ijmultiphaseflow.2010.09.010>
- Koffman, L.D., Plesset, M.S.: Experimental observations of the microlayer in vapor bubble growth on a heated solid. *J. Heat Transf.* **105**(3), 625 (1983). <https://doi.org/10.1115/1.3245631>
- Schweikert, K., Sielaff, A., Stephan, P.: On the transition between contact line evaporation and microlayer evaporation during the dewetting of a superheated wall. *Int. J. Therm. Sci.* **145**, 106025 (2019). <https://doi.org/10.1016/j.ijthermalsci.2019.106025>
- Schweizer, N.: Multi-scale investigation of nucleate boiling phenomena in microgravity. PhD thesis, Technische Universität, Darmstadt (2010)
- Sielaff, A.: Experimental investigation of single bubbles and bubble interactions in nucleate boiling. PhD thesis, Technische Universität, Darmstadt (2014)
- Sodtke, C., Kern, J., Schweizer, N., Stephan, P.: High resolution measurements of wall temperature distribution underneath a single vapor bubble under low gravity condition. *Int. J. Heat Mass Transf.* **49**, 1100–1106 (2006)
- Stephan, P., Hammer, J.: A new model for nucleate boiling heat transfer. *Heat Mass Transf.* **30**(2), 119–125 (1994)
- Straub, J., Zell, M., Vogel, B.: Boiling under microgravity conditions. In: Proceedings of the First European Symposium in Space, p 269 (1992)
- Tóth, B.: Development Operations teams, ESA’s Science Management, Payload and Teams, Science and Industry, Space: Future experiments to measure liquid-gas phase change and heat transfer phenomena on the international space station. *Microgravity Science Technol* **24**(3), 189–194 (2012)
- Utaka, Y., Hu, K., Chen, Z., Morokuma, T.: Measurement of contribution of microlayer evaporation applying the microlayer volume change during nucleate pool boiling for water and ethanol. *Int. J. Heat Mass Transf.* **125**, 243–247 (2018). <https://doi.org/10.1016/j.ijheatmasstransfer.2018.04.044>
- Wagner, E., Sodtke, C., Schweizer, N., Stephan, P.: Experimental study of nucleate boiling heat transfer under low gravity conditions using tics for high resolution temperature measurements. *Heat Mass Transf.* **42**(10), 875–883 (2006)

Publisher’s Note Springer Nature remains neutral with regard to jurisdictional claims in published maps and institutional affiliations.